Selective Use of Appropriate Image Pairs for Shape from Multiple Motions based on Gradient Method

Norio Tagawa and Syouta Tsukada
Graduate School of System Design, Tokyo Metropolitan University, 6-6- Asahigaoka, Hino, Tokyo, Japan

Keywords: Shape from Motion, Gradient Method, Direct Recovery, Random Camera Motions.

Abstract: For the gradient-based shape from motion, relative motions with various directions at each 3-D point on a target object are generally effective for accurate shape recovery. On the other hand, a proper motion size exists for each 3-D point having an intensity pattern and a depth that varied in each, i.e., a too large motion causes a large error in depth recovery as an alias problem, and a too small motion is inappropriate from the viewpoint of an SNR. Application of random camera rotations imitating involuntary eye movements of a human eyeball has been proposed, which can generate multiple image pairs. In this study, in order to realize accurate shape recovery, we improve the gradient method based on the multiple image pairs by selecting appropriate image pairs to be used. Its effectiveness is verified through experiments using the actual camera system that we developed.

1 INTRODUCTION

3D reconstruction from 2D images is a fundamental subject in the research field of the computer vision. There are various clues for reconstruction, for example, stereo (Lazaros et al., 2008), motion (Azevedo, 2006), shading (Samaras et al., 2000) and voxel coloriing (Seitz and Dyer, 1997). Shape from Motion (SfM) has attracted attention in particular. For the gradient-based shape from motion, a large amount of studies have been performed (Bruhn and Weickert, 2005), (Brox and Malik, 2011), (Ochs and Brox, 2012). To avoid occlusions for point correspondences between images, we have focused on a monocular stereo vision. The gradient-based method using the relation between spatiotemporal differentials of image intensity and an optical flow field has attracted attention because of its analytic formulation property. The method is effective for a small motion parallax between successive two images, hence it cannot execute high accurate recovery in general.

One strategy for high accuracy is the use of multiple images observed from various viewpoints. When we use the camera moving continuously around a target object, corresponding points in an image sequence are required to be tracked, which is also a difficult task of the computer vision. Therefore, a method using multiple images without the tracking is desired. As such a method, we have proposed the depth recovery using random camera rotations imitating fixational eye movements of a human's eye ball (Tagawa, 2010). The rotation center of the camera rotations is set at the back of a lens center. Such a rotation causes a translational motion of a lens center, which indicates that depth information can be observed. Since the camera rotations cause small image motions having various direction, a lot of image pairs are generated and can be used simultaneously for the gradient-based method without point correspondence by tracking.

On the other hand, the accuracy of the gradient-based method is mainly affected by the equation error of the gradient equation. The gradient equation is derived as a first order approximation of the intensity invariant constraint before and after the relative motion between a camera and a target object. Hence, the second and more higher order terms corresponds to the equation error. The degree of the error is determined by the relation between the size of the optical flow and the spatial frequency of a dominant intensity pattern.

To reduce the influence of such an equation error, the optimal frequency component was extracted at each pixel and was used for depth recovery (Tagawa and Koizumi, 2015). In this method, all observed motions caused by random camera rotations are used at all pixels by tuning the image resolution to each motion at every pixel. When a lot of image pairs are observed and can be used for recovery, the strategy

Tagawa, N. and Tsukada, S.
Selective Use of Appropriate Image Pairs for Shape from Multiple Motions based on Gradient Method.
DOI: 10.5220/0005778805520561
In *Proceedings of the 11th Joint Conference on Computer Vision, Imaging and Computer Graphics Theory and Applications (VISIGRAPP 2016) - Volume 3: VISAPP*, pages 554-563
ISBN: 978-989-758-175-5

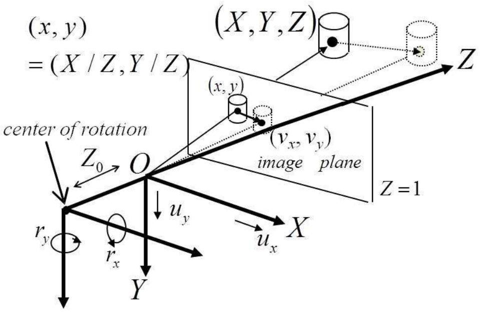

Figure 1: Coordinate system and camera motion model used in this study.

in which at least one frequency component is used at every successive image pair (Tagawa and Koizumi, 2015) seems to be redundant, i.e., it is not necessary to extract the optimal resolution for every motion. It is expected that the method which selects the appropriate image pairs, i.e., appropriate image motions generally called optical flows, having little high order terms in the gradient equation at every pixel also can reduce the equation error. In this study, the effectiveness of the selective use of the appropriate image pairs is confirmed through real image experiments.

In the following, the method (Tagawa, 2010) used as a fundamental framework in this study is explained briefly in Sec. 2, and the proposed technique to select the appropriate image pairs at each pixel is introduced in Sec. 3. Experimental results using real images are shown to reveal the effectiveness in Sec. 4, and the problems left for the future are discussed in Sec. 5.

2 DEPTH FROM MULTIPLE IMAGES

2.1 Projection and Motion of Camera

The camera coordinate and the camera motion model are shown in Fig. 1. A perspective projection is adopted, and a 3D point $(X,Y,Z)^\top$ on an object is projected into an image point $x \equiv (x,y,1)^\top = (X/Z,Y/Z,1)^\top$. A camera rotation center is set at the back of a lens center with a distance of Z_0 along an optical axis. A rotation identified by a rotational velocity vector $r = [r_X, r_Y, r_Z]^\top$ causes the rotation of a lens center which is represented with the same value of r. A translation is not applied explicitly, but the rotation of which the rotation axis is different from a lens center causes a translation of a lens center implicitly. The translational velocity vector $u = [u_X, u_Y, u_Z]^\top$ is formulated as follows:

$$\begin{bmatrix} u_X \\ u_Y \\ u_Z \end{bmatrix} = \begin{bmatrix} r_X \\ r_Y \\ r_Z \end{bmatrix} \times \begin{bmatrix} 0 \\ 0 \\ Z_0 \end{bmatrix} = Z_0 \begin{bmatrix} r_Y \\ -r_X \\ 0 \end{bmatrix}. \quad (1)$$

If we know the value of Z_0, an absolute shape of an object can be recovered, although by a general camera motion only a relative shape is recovered.

Equation 1 indicates that r_Z is not required to generate the translation, hence a 2D rotational velocity $r = [r_X, r_Y]^\top$ can be redefined and used for recovery. $r^{(j)}$ indicates the discrete value of r in the jth image pair. Because the use of various optical flows is effective for the accurate shape recovery, $\{r^{(j)}\}$ is desired to be a random number series. To avoid feature tracking, the camera is required to randomly rotates around the optical axis without the divergence of the camera direction. In order to put such a rotation into practice, the random series of the rotational velocity which corresponds to the small rotation between successive images in a discrete system is required to have a time correlation. This indicates that the random camera rotations should be modeled, for example, as an autoregressive (AR) series. In this study, for simplicity, we assume that $r^{(j)}$ is a sample of the 2D Gaussian white random variable.

$$p(\{r^{(j)}\}_{j=1}^{M} | \sigma_r^2) = \frac{1}{(\sqrt{2\pi}\sigma_r)^{2M}} \exp\left\{ -\frac{\sum_{j=1}^{M} r^{(j)\top} r^{(j)}}{2\sigma_r^2} \right\}. \quad (2)$$

In our experiments, firstly we generate the random number series of an absolute camera direction according to the 2D Gaussian white random variable with an average of 0 and a variance of σ^2, and use it to rotate a camera. Therefore, the difference of the camera direction series, which is treated as an unknown variable, corresponds to $r^{(j)}$. Although $\{r^{(j)}\}$ is a colored series actually, we approximate its probability density with Eq. 2 using $\sigma_r^2 = 2\sigma^2$

2.2 Depth Recovery

For the camera motion explained in Sec. 2.1, the optical flow $v \equiv [v_x, v_y]^\top$ is formulated as follows:

$$v_x = xyr_x - (1+x^2)r_y + yr_z - Z_0 r_y d \equiv v_x^r - r_y Z_0 d, \quad (3)$$

$$v_y = (1+y^2)r_x - xyr_y - xr_z + Z_0 r_x d \equiv v_y^r + r_x Z_0 d, \quad (4)$$

where $d \equiv 1/Z$ is an inverse depth.

The gradient equation, a first-order approximation of the intensity invariant constraint before and after the camera motion, is derived as follows:

$$f_t = -f_x v_x - f_y v_y, \quad (5)$$

where $f(x,y,t)$ is an image intensity, and f_x, f_y, f_t are the partial derivatives of f, where (x,y) is a coordinate system in an image plane and t indicates time. The gradient equation is applied to a successive image pair, in principle. By substituting Eqs. 3 and 4 into Eq. 5, the gradient equation for a rigid object with the camera rotations in Sec. 2.1 is derived.

$$f_t = -(f_x v_x^r + f_y v_y^r) - (-f_x r_y + f_y r_x) Z_0 d \equiv -f^r - f^u d. \tag{6}$$

Using Eq. 6, the inverse depth can be directly recovered without optical flow detection. This scheme is effective for shape from multiple images, since the inverse depth can be considered as a common variable for all image pairs.

We assume that $f_t^{(i,j)}$, where i and j are a pixel position and a frame number respectively, includes an observation error according to the Gaussian distribution with an average of 0 and a variance of σ_o^2, but $f_x^{(i,j)}$ and $f_y^{(i,j)}$ have no errors. We consider that the equation error of the gradient equation is dominant in the error of $f_t^{(i,j)}$.

In addition, $\{d^{(i)}\}$ should be assumed to have local correlation spatially, since an object usually has a smooth structure. As a simple modeling, we use the following prior of $\{d^{(i)}\}$.

$$p(d|\sigma_d^2) = \frac{1}{(\sqrt{2\pi}\sigma_d)^N} \exp\left\{-\frac{d^\top L d}{2\sigma_d^2}\right\}, \tag{7}$$

where d is an N-dimensional vector consisting of $\{d^{(i)}\}$, where N indicates the number of pixels, and L indicates the matrix corresponding to the 2D Laplacian operator, and we control σ_d^2 heuristically in consideration of the smoothness of a recovered depth map.

Based on the probabilistic models of $\{r^{(j)}\}$, $\{f_t^{(i,j)}\}$ and $\{d^{(i)}\}$ defined above, we can statistically estimate the inverse depth map. By applying the MAP-EM algorithm (Dempster et al., 1977), σ_o^2 and $\{d^{(i)}\}$ are determined as a MAP estimator based on $p(d, \sigma_o^2 | \{f_t^{(i,j)}\})$ and $\{r^{(j)}\}$ is also determined as a MAP estimator from $p(\{r^{(j)}\} | \{f_t^{(i,j)}\}, \hat{\sigma_o}^2, \{\hat{d}\})$, in which $\hat{}$ means a MAP estimator. It is noted that the uniform distribution should be used as the prior of σ_o^2, because of no information of σ_o^2 in advance. The details of the estimation algorithm are shown in the literature (Tagawa, 2010), in which σ_r^2 is also estimated, but in this study, it is assumed to be known as a setting value.

3 SELECTION OF IMAGE PAIRS FOR ACCURATE RECOVERY

Based on the condition that many image pairs are available, we propose a scheme that at every pixel we discard the gradient equations, i.e. discard the image pairs having a large approximation error. In each pixel, we decide which image pair should be discarded.

At the first step, we focus on an alias problem. An alias in signal processing is a state caused by a low sampling rate as compared with the maximum frequency of signals. In this study, when an image motion between two images is large against the spatial wavelength of a dominant image intensity pattern, the direction of the detected optical flow is opposite to the true direction and causes a large recovery error of a depth map. In the image region where the alias occurs, the angle between the spatial gradient vectors of successive image pairs $f_s^{(i,j)}$ and $f_s^{(i,j+1)}$, where $f_s^{(i,j)} = [f_x^{(i,j)}, f_y^{(i,j)}]^\top$, tends to be large. Therefore, the angle defined by both vectors can be used to find the alias region. The image pairs in which the angle is large should be detected in each pixel and discarded thresholding.

In the next step, we further select the appropriate image pairs independently in each pixel from the image pairs remained through the first step described above in consideration of the amount of nonlinear terms included in the observation of f_t. The exact f_t is represented as follows:

$$f_t = -f_x v_x - f_y v_y - \frac{1}{2}\left\{f_{xx} v_x^2 + f_{yy} v_y^2 + 2 f_{xy} v_x v_y\right\} + \cdots \tag{8}$$

After discarding the exceedingly inappropriate image pairs by the first step, the nonlinear term can be considered small, and the second order term in Eq. 8 can be approximated at every pixel i as follows:

$$-\frac{1}{2}\left\{(f_x^{(i,j)} - f_x^{(i,j+1)}) v_x^{(i,j)} + (f_y^{(i,j)} - f_y^{(i,j+1)}) v_y^{(i,j)}\right\}. \tag{9}$$

This representation can be introduced from the following gradient equations with respect to f_x and f_y,

$$f_{xx} v_x + f_{xy} v_y + f_{xt} = 0, \tag{10}$$

$$f_{yx} v_x + f_{yy} v_y + f_{yt} = 0, \tag{11}$$

with the approximations of $f_{xt} \approx f_x^{(i,j+1)} - f_x^{(i,j)}$ and $f_{yt} \approx f_y^{(i,j+1)} - f_y^{(i,j)}$. Equation 9 can be computed without detecting the second derivatives of f, which tend to be noisy.

In this step, we take into account the SNR of f_t. When optical flow is small relative to a dominant intensity pattern, the first term in Eq. 8 is likely to be small. Inversely when optical flow is large, the term in Eq. 9 tends to be large. Those means that the SNR may lowers, if a camera motion is too small or too large. To estimate the SNR of the observed f_t, we can define the measure J_o as a ratio of the value of Eq. 9 and the first order term of Eq. 8.

$$J_o \equiv \frac{|(f_x^{(i,j)} - f_x^{(i,j+1)})v_x^{(i,j)} + (f_y^{(i,j)} - f_y^{(i,j+1)})v_y^{(i,j)}|}{2|f_x^{(i,j)}v_x^{(i,j)} + f_y^{(i,j)}v_y^{(i,j)}|}. \tag{12}$$

It can be easily known that J_o depends on the direction of optical flow but is invariant with respect to the amplitude of optical flow. Additionally, even if the difference of the spatial gradients $f_s^{(i,j)} - f_s^{(i,j+1)}$ is large, when the direction of $f_s^{(i,j)} - f_s^{(i,j+1)}$ is perpendicular to the direction of optical flow, the value of J_o becomes small. Therefore, the value $J \equiv |f_s^{(i,j)} - f_s^{(i,j+1)}|/|f_s^{(i,j)}|$ can be used as a worst value of J_o, which can be computed without the true value of optical flow. In this study, the image pairs for which the value of J is less than the certain threshold are selected in each pixel to be used for depth recovery.

For the image pairs finally selected independently in each pixel, the gradient equation including the second order term is redefined as follows:

$$\begin{aligned} f_t^{(i,j)} &= -f_x^{(i,j)}v_x^{(i,j)} - f_y^{(i,j)}v_y^{(i,j)} \\ &-\frac{1}{2}\left\{(f_x^{(i,j)} - f_x^{(i,j+1)})v_x^{(i,j)} + (f_y^{(i,j)} - f_y^{(i,j+1)})v_y^{(i,j)}\right\} \\ &= -\frac{3f_x^{(i,j)} - f_x^{(i,j+1)}}{2}v_x^{(i,j)} - \frac{3f_y^{(i,j)} - f_y^{(i,j+1)}}{2}v_y^{(i,j)}. \end{aligned} \tag{13}$$

In the following experiments, Eq. 13 is used instead of Eq. 5.

4 EXPERIMENTS

4.1 Camera System

The developed camera system used to perform the experiments of this study is shown in Fig. 2 with a target object. The camera system can be rotated around the horizontal axis i.e. X axis and around the vertical axis, i.e. Y axis. The rotation around the optical axis, i.e. Z direction, cannot be performed, which is not needed to obtain the depth information. The parameters of the system are shown as follows:

- Focal length: 2.8 – 5.0 mm
- Image size: 2 million (1200 × 1600) pix.

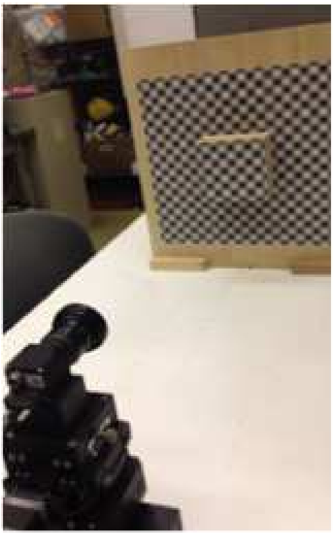

Figure 2: Camera system with target object.

- Movable range:
  X-axis 360 deg., Y-axis $(-10, +10)$ deg.
- Minimum moving unit:
  X-axis 1 pulse = 0.01 deg.,
  Y-axis 1 pulse = 0.00067 deg.
- Image property: 8 or 12 bit grayscale

While rotating the camera according to the rotation data explained in Sec. 2.1, the computer captures images automatically.

4.2 Results

We explain the results of the experiments using the real images captured by the developed camera system. The images are gray scale and consist of 256 × 256 pixels with 8 bit digitization. An example is shown in Fig. 3(a). Before experiments, a focal length of 1141 pixel was measured by the conventional calibration method (Zhang, 2000). Our camera system has a parallel stereo function, namely the camera can be moved laterally by a slide system. The depth map recovered by the stereopsis is shown in Fig. 3(b). In this figure, the horizontal axis indicates a position in the image plane, and the vertical axis indicates a depth value. The back board of the target object is 191.3 mm away from the lens center and the front board in the center part is 141.5 mm. In the stereopsis, 10 points in an image were selected as a feature point for each of back board region and the front board region respectively, and were used for depth computing. The average of the depth of each 10 points was computed to determine the depth of the plane board. Z_0 was also measured with 38.8 mm using the above depth value

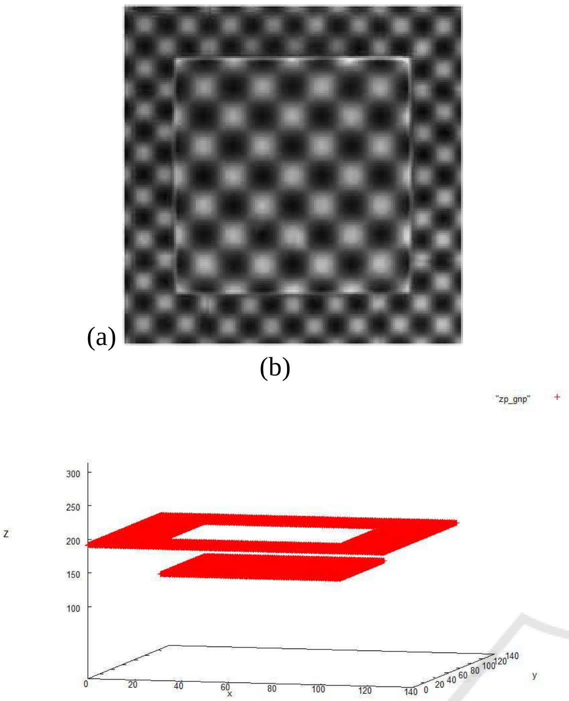

Figure 3: Data used for experiments: (a) example of captured image, (b) depth map recovered by binocular stereopsis.

of the object. The calibration algorithm for Z_0 is explained in the APPENDIX.

100 images were captured for each setting value of $\sigma_r^2[\mathrm{rad}^2]$ and were used for recovery. We varied σ_r^2 as 6.13×10^{-6}, 2.32×10^{-5} and 9.39×10^{-5}, by each of which the average of the amplitude of the optical flow approximately coincides with $\lambda/8$, $\lambda/4$ and $\lambda/2$ respectively, where λ indicates the wavelength of the dominant intensity pattern. The smoothness parameter of a depth map, σ_d^2, was set as 1.0×10^{-4} heuristically.

The combination of two threshold values required for the two selection steps explained in Sec. 3 respectively has to be carefully examined in the future study, which includes the determination method of the threshold values. In this study, we heuristically use the combination of the threshold values shown in Table1. The threshold value in the second step corresponds to the multiplying factor of the J's average about pixels selected by the first step in the region of the front board of the target. Hence, for example, the threshold value 2 is equivalent to twice the average. The J's average used as an unit as above changes by the value of σ_r^2: 0.594 for $\sigma_r^2 = 6.13 \times 10^{-6}$, 0.963 for $\sigma_r^2 = 2.33 \times 10^{-5}$ and 1.297 for $\sigma_r^2 = 9.39 \times 10^{-5}$.

The reason why the threshold value in the first step is increased depending on the threshold value in the second step is that since the second step selection using a large threshold value can permit the selection of the image pairs having a large high-order terms, a severe limit by the first step may remove the effect of the second step. However, when the limitation achieved by the first step is loose, the definition of J, which is introduced by assuming that the higher-order terms in Eq. 8 is small, may not be reliable.

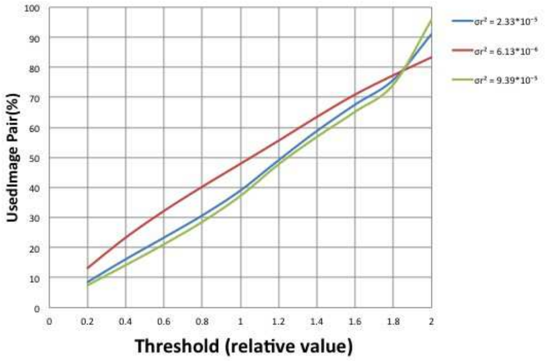

Figure 4: Relation between usage rate of image pairs and threshold for J, i.e. for second step. Blue line indicates $\sigma_r^2 = 6.13 \times 10^{-6}$, red line indicates $\sigma_r^2 = 2.32 \times 10^{-5}$ and green line indicates $\sigma_r^2 = 9.39 \times 10^{-5}$.

Table 1: Combination of threshold values of first and second steps for image pairs selection.

First (deg.)	18	36	54	72	90	108	126	144	162	180
Second (relative)	0.2	0.4	0.6	0.8	1.0	1.2	1.4	1.6	1.8	2.0

The relation between the thresholding and the usage rate of the image pairs in the experiments is shown in Fig. 4 for the above mentioned three values of σ_r^2. The threshold value of the second step is used in the horizontal axis. The usage rate in the vertical axis means the average for all pixels of the rate of the finally selected image pairs in each pixel. The usage rate increases in proportion to the threshold value regardless of the value of σ_r^2. It is noted that the ratio of the image pairs of which the angle of the spatial gradient vectors is larger than 90 deg. at every pixels with respect to the total number, i.e. $N^2 \times (M-1) = 256^2 \times 99$ are 16.6% for $\sigma_r^2 = 6.13 \times 10^{-6}$, 38.4% for $\sigma_r^2 = 2.32 \times 10^{-5}$ and 52.2% for $\sigma_r^2 = 9.39 \times 10^{-5}$. In the future study, we are planning that in the first step for the image pairs selection, the image pairs with the angle being larger than 90 deg. are totally discarded.

It can be confirmed also from Fig. 4 that when we use image pairs of the same quantity for all three of σ_r^2, the selected image pairs for $\sigma_r^2 = 2.32 \times 10^{-5}$ and $\sigma_r^2 = 9.39 \times 10^{-5}$ may include much high order components more than those for $\sigma_r^2 = 2.32 \times 10^{-5}$. This may cause the difference in the accuracy of recovery

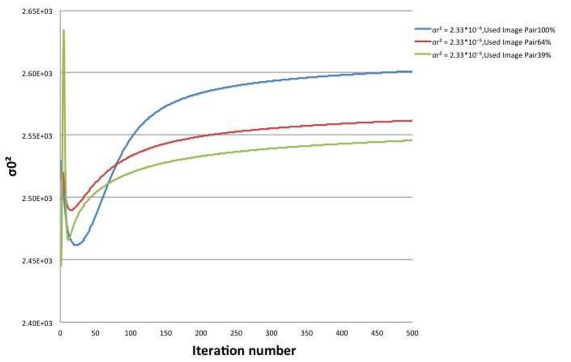

Figure 5: Convergence process of σ_o^2 in iteration of MAP-EM algorithm with $\sigma_r^2 = 2.32 \times 10^{-5}$. Blue line indicates usage rate= 100%, red line indicates usage rate= 64% and green line indicates usage rate= 39%.

by σ_r^2.

Figure 5 shows the convergence process of σ_o^2 in the MAP-EM algorithm with $\sigma_r^2 = 2.32 \times 10^{-5}$. As a matter of course, the convergence value of σ_o^2 is small so that the usage rate is low.

The recovered depth maps with a small motion, i.e. $\sigma_r^2 = 6.13 \times 10^{-6}$, using all image pairs are shown in Fig. 6, in which a 3D representation and a cross-sectional representation of the center region are shown as (a) and (b) respectively. The result with middle motion, i.e. $\sigma_r^2 = 2.32 \times 10^{-5}$, using all image pairs are also shown in Fig. 7. For the large motion, i.e. $\sigma_r^2 = 9.39 \times 10^{-5}$, depth recovery using all image pairs has a large recovery error, and hence it is omitted here. By comparing both results in Figs. 6 and 7 indicate that, although too small camera motion is expected to cause no aliases, the generated depth information is very poor. However, even if the motion becomes larger, enough improvement of the accuracy cannot be achieved as far as we use all image pairs.

Figures 8, 9 and 10 show the recovered depth with the selective use of appropriate image pairs as a cross-sectional representation. From these figures, we can confirm that the accuracy of recovery strongly depends on the usage rate of image pairs. We can also understand that the appropriate usage rate exists. This tendency is confirmed also from Fig. 11 indicating the RMSE (root mean square error) of the recovered depth. For each motion size, the depth map recovered comparatively well is shown in Figs. 12, 13 and 14 respectively.

It is confirmed from Fig. 11 that selecting the appropriate image pairs is effective for all values of σ_r^2, but still, the suitable camera rotations with respect to the spatial frequency of the object's texture are desirable as a whole. In the experiments, the motion corresponding to $\sigma_r^2 = 2.32 \times 10^{-5}$, i.e. middle motion is optimal.

(a)

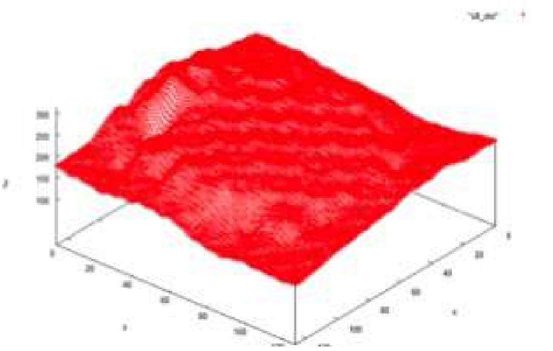

(b)

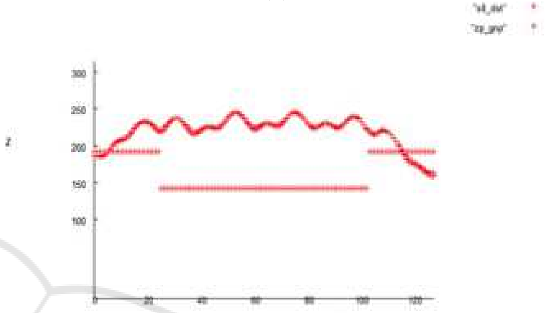

Figure 6: Depth recovered without selective use of image pairs for $\sigma_r^2 = 6.13 \times 10^{-6}$: (a) 3D map, (b) cross-sectional representation.

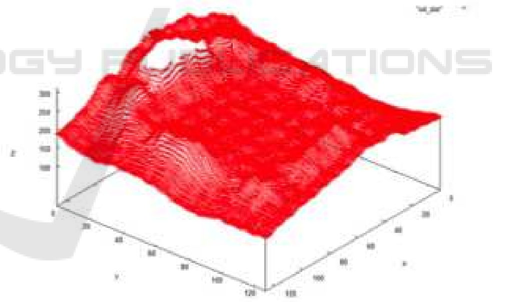

(a)

(b)

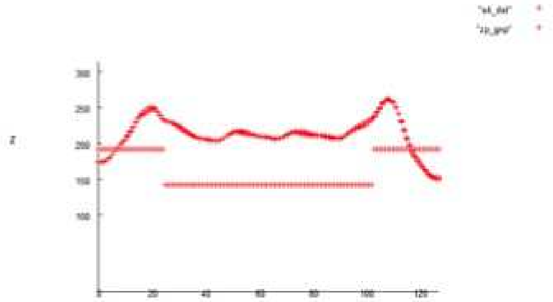

Figure 7: Depth recovered without selective use of image pairs for $\sigma_r^2 = 2.32 \times 10^{-5}$: (a) 3D map, (b) cross-sectional representation.

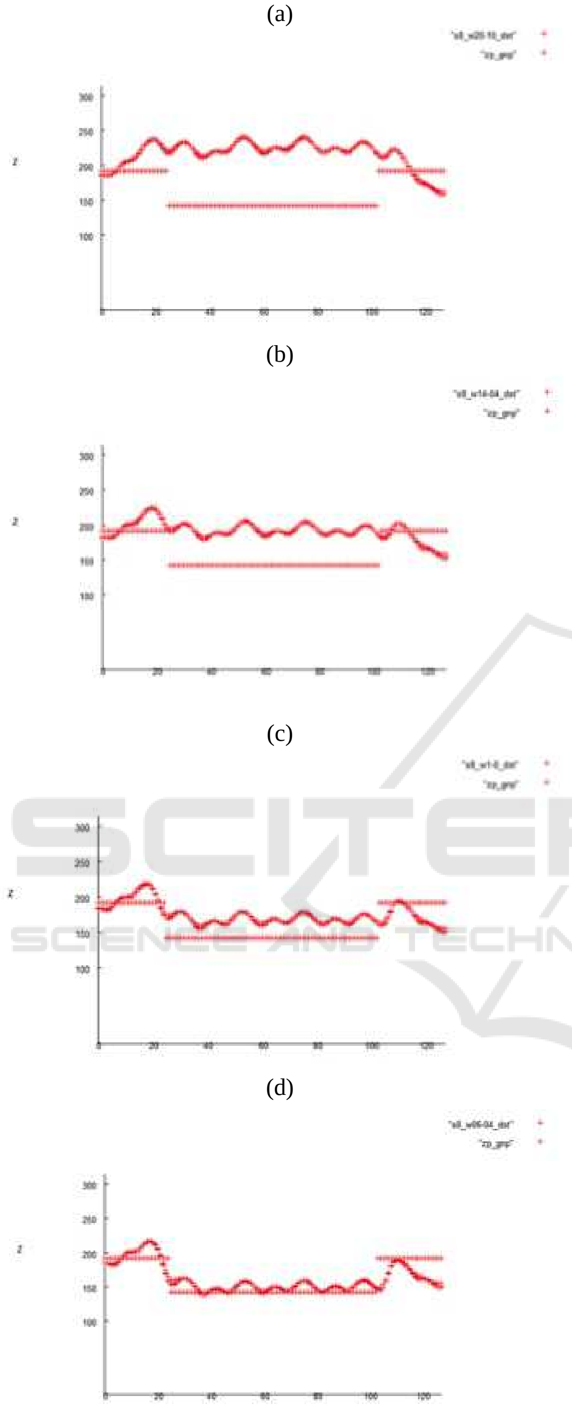
(a)

(b)

(c)

(d)

Figure 8: Depth recovered with image pair selection for $\sigma_r^2 = 6.13 \times 10^{-6}$ with cross-sectional representation:(a) usage rate of 83%; (b) 64%; (c) 48%; (d) 32%.

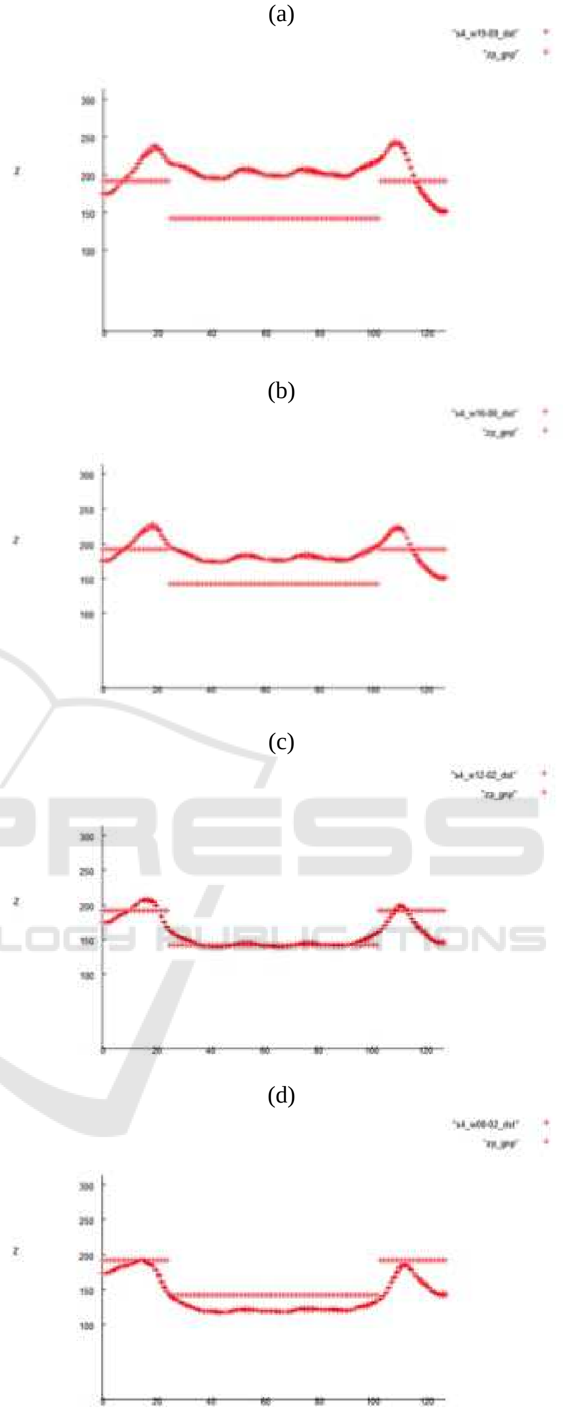
(a)

(b)

(c)

(d)

Figure 9: Depth recovered with image pair selection for $\sigma_r^2 = 2.32 \times 10^{-5}$ with cross-sectional representation: (a) usage rate of 83%; (b) 68%; (c) 49%; (d) 31%.

The reason can be expected as follows: From Fig. 11, the image pairs obtained by the motion according to $\sigma_r^2 = 2.32 \times 10^{-5}$ includes good image pairs with approximately 60%. Each of such image pairs has the motion size of which is in the specific range. However, the image pairs generated by a motion with $\sigma_r^2 = 6.13 \times 10^{-6}$ or those with $\sigma_r^2 = 9.39 \times 10^{-5}$ does not include enough quantity of such

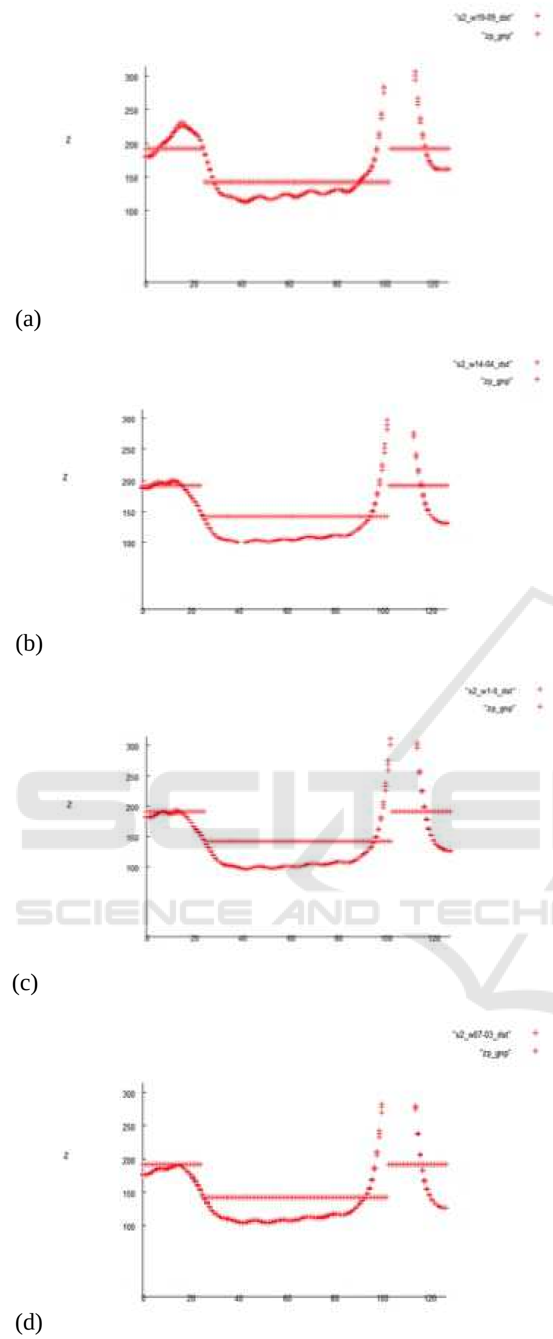

(a)

(b)

(c)

(d)

Figure 10: Depth recovered with image pair selection for $\sigma_r^2 = 9.39 \times 10^{-5}$ with cross-sectional representation:(a) usage rate of 80%; (b) 56%; (c) 37%; (d) 25%.

a suitable motion. In addition, for $\sigma_r^2 = 6.13 \times 10^{-6}$ or $\sigma_r^2 = 9.39 \times 10^{-5}$, if we select image pairs having such a motion included in the suitable range by adjusting the threshold values, the number of the selected image pairs decreases and hence, the accuracy of recovery tends to lower.

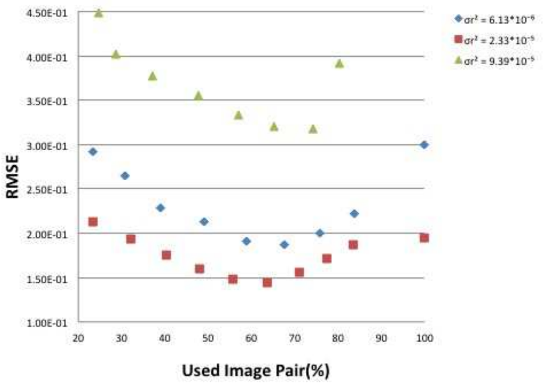

Figure 11: RMSE of recovered depth against use rate of image pairs. Blue pot is $\sigma_r^2 = 6.13 \times 10^{-6}$, red plot is $\sigma_r^2 = 2.32 \times 10^{-5}$ and green plot is $\sigma_r^2 = 9.39 \times 10^{-5}$.

Since the suitable size of optical flow is determined with respect to an wavelength of a dominant intensity pattern, and the size of optical flow changes according to the depth from the camera, the camera motion averagely suitable for whole image depends on a dominant texture and an averaged depth of a target object. After using such a camera motion, the appropriate image pairs have to be selected independently in each pixel, since a texture is not unique on an object and local adjustment of optical flow used for recovery should be performed by the proposed selective use technique.

As stated above, in the strategy in which appropriate image pairs are selected from the limited number of images, random camera motions having a variation that is suited on the average for the texture and the depth of a target object has to be determined in advance. However, it is difficult practically. To avoid the problem, if the optimal threshold values can be known as a constant, we should determine whether each image pair should be used or not as an online operation for obtaining enough amount of image pairs while acquiring images continuously.

5 CONCLUSIONS

In this study, we proposed a technique to select the appropriate image pairs, and confirmed its effectiveness through experiments using the developed camera system. The results assert that the gradient equation having a large amount of high order components should be discarded to improve the accuracy.

In the future work, the following tasks should be solved.

- Optimal thresholding process
  As described in Sec. 4.2, we have to examine

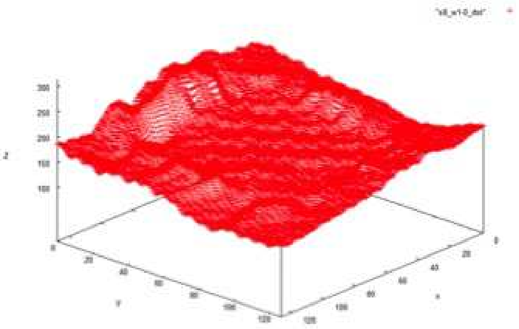

Figure 12: 3D representation of recovered depth for $\sigma_r^2 = 6.13 \times 10^{-6}$ with usage rate of 48%.

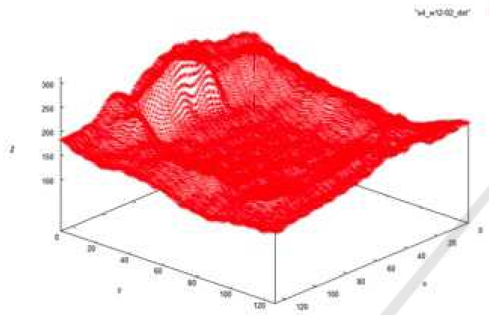

Figure 13: 3D representation of recovered depth for $\sigma_r^2 = 2.32 \times 10^{-5}$ with usage rate of 49%.

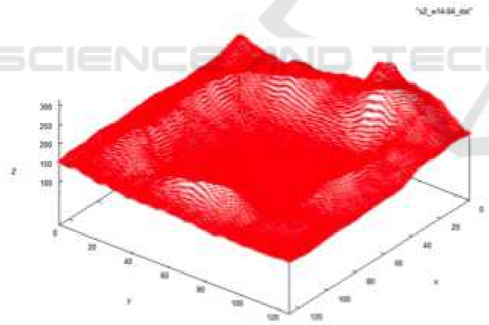

Figure 14: 3D representation of recovered depth for $\sigma_r^2 = 9.39 \times 10^{-5}$ with usage rate of 56%.

the method to combine the two steps for image pairs selection. Since the first step is required to simply evaluate the SNR using $J = |f_s^{(i,j)} - f_s^{(i,j+1)}|/|f_s^{(i,j)}|$ which is used in the second step, we should fix the threshold value in the first step regardless of the second step. The optimal threshold value in the second step is expected to be determined by the prior simulations using artificially generated images having various intensity patterns. The relation between the SNR of f_t and the threshold value should be clarified. On the other hand, we will evaluate the approximation error obtained in Eq. 9 with respect to the second order term in Eq. 8. Additionally, the relation between J_o and J, which is a worst value of J_o, will be examined in order to confirm the effect using J instead of J_o.

- Camera Motion Estimation
  We have to examine the influence on the accuracy of the estimate of $\{r^{(j)}\}$ due to discarding observations partially, and ease it if it may be severe. In the MAP-EM algorithm, $\{r^{(j)}\}$ is expected to be randomly sampled according to the density of Eq. 2, but after discarding some wrong image pairs, rs observed and used for depth recovery may have a bias. Even if $\{r^{(j)}\}$ is a random variable set according to the Gaussian distribution, those selected and used for recovery may be modeled appropriately by the other distribution. In addition, we should examine the approximation error of the density of $\{r^{(j)}\}$. In this study, the correlation between $r^{(j)}$ and $r^{(j-1)}$ is ignored.

- Depth Modeling
  We have to modify the 2D Laplacian matrix used in the prior of $\{d^{(i)}\}$ in Eq. 7 so as to take into account the discontinuity of an object. If we detect a object edge in advance, the 2D Laplacian matrix can be easily revised using such a edge information. Alternatively, a line process or a region variable can be additionally introduced, though the computation is complicated.

REFERENCES

Azevedo, T. (2006). Development of a computer platform for object 3d reconstruction using computer vision techniques. In *proc. Conf. Comput. Vision, Theory and Applications*, pages 383–388.

Brox, T. and Malik, J. (2011). Large displacement optical flow: descriptor matching in variational motion estimation. *IEEE Trans. Pattern Anal. Machine Intell.*, 33(3):500–513.

Bruhn, A. and Weickert, J. (2005). Lucas/kanade meets horn/schunk: combining local and global optic flow methods. *Int. J. Comput. Vision*, 61(3):211–231.

Dempster, A. P., Laird, N. M., and Rubin, D. B. (1977). Maximum likelihood from incomplete data. *J. Roy. Statist. Soc. B*, 39:1–38.

Lazaros, N., Sirakoulis, G. C., and Gasteratos, A. (2008). Review of stereo vision algorithm: from software to hardware. *Int. J. Optomechatronics*, 5(4):435–462.

Ochs, P. and Brox, T. (2012). Higher order motion models and spectral clustering. In *proc. CVPR2012*, pages 614–621.

Samaras, D., Metaxas, D., Fua, P., and Leclerc, Y. G. (2000). Variable albedo surface reconstruction from stereo and shape from shading. In *proc. Int. Conf. CVPR*, volume 1, pages 480–487.

Seitz, S. M. and Dyer, C. M. (1997). Photorealistic scene reconstruction by voxel coloring. In *proc. Int. Conf. CVPR*, pages 1067–1073.

Tagawa, N. (2010). Depth perception model based on fixational eye movements using byesian statistical inference. In *proc. Int. Conf. Pattern Recognition*, pages 1662–1665.

Tagawa, N. and Koizumi, S. (2015). Selective use of optimal image resolution for depth from multiple motions based on gradient scheme. In *proc. Int. Workshop on Image Mining. Theory and Applications*, pages 92–99.

Zhang, Z. (2000). A flexible new technique for camera calibration. *IEEE Trans. Pattern Anal. Machine Intell.*, 22(11):1330–1334.

APPENDIX

We recover the object shape by a binocular stereopsis, and assume that the 3D point X_1 on the object measured from the coordinate associated with a reference camera position shown in Fig. 15 corresponds to the image position $x_1 = [x_1, y_1, 1^\top]$. The same 3D point is represented as X_2 with the coordinate after rotated around the x-axis with a rotation matrix $\mathbf{R}$,

$$\mathbf{R} = \begin{bmatrix} 1 & 0 & 0 \\ 0 & \cos\theta & -\sin\theta \\ 0 & \sin\theta & \cos\theta \end{bmatrix}. \tag{14}$$

By the rotation, the lens center is translated as T, which can be represented using the reference coordinate as follows:

$$\begin{aligned} T &= Z_0 z_2 - Z_0 z_1 \\ &= Z_0 \mathbf{R} z_1 - Z_0 z_1 \\ &= Z_0 \left(\mathbf{R} - \mathbf{I}\right) z_1 \\ &\equiv Z_0 \mathbf{S} z_1, \end{aligned} \tag{15}$$

where $z_1 = [0, 0, 1]^\top$. The relation between X_1 and X_2 is formulated as,

$$\mathbf{R} X_2 = X_2 - T. \tag{16}$$

By assuming that x_2 corresponds to x_1 and the position of them are known in each image, we can use the following equations.

$$x_1 = \frac{X_1}{Z_1}, \qquad x_2 = \frac{X_2}{Z_2}, \tag{17}$$

where Z_2 is unknown. From those formulations, the next equation is derived.

$$Z_2 \mathbf{R} x_2 = X_1 - Z_0 \mathbf{S} z_1. \tag{18}$$

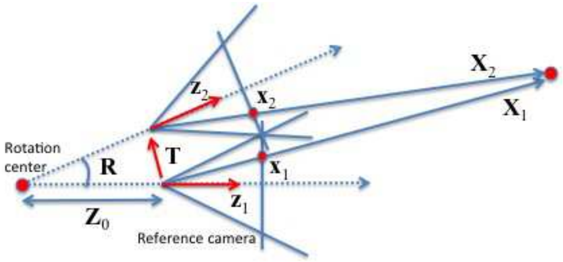

Figure 15: Geometric illustration for determining Z_0.

This equation is rewritten with components as follows:

$$Z_2 \begin{bmatrix} x_2 \\ y_2\cos\theta - \sin\theta \\ y_2\sin\theta + \cos\theta \end{bmatrix} = \begin{bmatrix} X_1 \\ Y_1 + Z_0\sin\theta \\ Z_1 - Z_0(\cos\theta - 1) \end{bmatrix}. \tag{19}$$

Using the second and the third rows, Z_0 can be solved as follows:

$$Z_0 = \frac{Z_1(y_2\cos\theta - \sin\theta) - Y_1(y_2\sin\theta + \cos\theta)}{\sin\theta(y_2\sin\theta + \cos\theta) + (\cos\theta - 1)(y_2\cos\theta - \sin\theta)}. \tag{20}$$